

Study of sub-GeV Dipolar Dark States at SND@LHC within Invisible Bounds on Meson Decays

Debajyoti Biswas^{1,*}

¹*Centre for High Energy Physics, Indian Institute of Science,
CV Raman Road, Bengaluru 560 012, India*

(Dated: January 7, 2026)

Abstract

Electromagnetic form factors constitute a natural portal for accessing states beyond the Standard Model. In particular, dimension-5 magnetic and electric dipole moment operators offer a minimal and predictive framework for Feebly Interacting Particles (FIPs). In this work, we perform a study of the sensitivity reach of the Scattering and Neutrino Detector (SND@LHC) in the detection of dipolar dark states through photon-mediated interactions with the Standard Model particles. The far-forward region of the LHC provides FIPs with large momenta that scatter off electrons and nuclei inside the target. Production of dark states from meson decays is constrained by invisible decay widths, while the Drell-Yan process offers a production channel in the GeV range. We present sensitivity plots for magnetic and electric dipole moment interactions at SND@LHC and compare them with constraints from direct detection, beam dump, fixed-target, and collider experiments. The validity of the effective theory that describes the dipole model is also studied by considering conservative bounds on the couplings.

* debajyotib@iisc.ac.in,

I. Introduction

Despite the remarkable success of the Standard Model in describing particle interactions at the electroweak scale, the absence of clear signals of new physics at high energies has motivated increasing interest in scenarios involving weakly coupled dark sectors. In many well-motivated extensions of the Standard Model, new degrees of freedom interact only feebly with ordinary matter, rendering them difficult to access in conventional collider searches. Such states are instead more naturally probed in high-intensity experiments, where large fluxes and momenta can compensate for small couplings. Experiments at the Forward Physics Facility [1–5] at the LHC and fixed-target facilities therefore offer sensitivity to sub-GeV new physics that is difficult to access with conventional central detectors.

Among these efforts, the Scattering and Neutrino Detector at the LHC occupies a distinct position. Although the SND@LHC is designed primarily to study neutrinos produced at the ATLAS interaction point, its geometry, target composition, and location close to the beam collision axis also render it sensitive to new particles whose dominant experimental signature arises from elastic scattering. Importantly, SND operates in a regime where neutrino backgrounds are measurable and can be constrained using data from the detector itself or from simulations performed.

In this work we focus on sub-GeV dark states interacting with the Standard Model through electromagnetic dipole operators. In the far-forward region of the LHC, dipolar dark states can be produced efficiently through meson decays, Drell-Yan process, and other photon-mediated pair production channels. Once produced, they may scatter in the detector material, yielding observable recoil signals that compete with neutrino-induced backgrounds. This interplay between production and scattering defines a region of parameter space where SND@LHC provides sensitivity complementary to that of other facilities.

The purpose of this work is to quantify the reach of SND@LHC for such dark states in a unified framework. In Section II, we introduce the dark state model considered in this study. Section III describes the layout of SND@LHC and presents a schematic overview of the detector along with a description of the key components relevant for the detection of neutrinos and FIPs. The results of simulations of neutrino backgrounds at the SND@LHC are also presented. In Section IV, we discuss the production channels relevant to our model, including meson decay widths and the resulting spectra of mesons and dark states. We com-

pute the production cross-section both in the forward hemisphere and in the pseudorapidity range covered by SND@LHC. Finally, in Section V, we derive constraints from invisible decay widths of mesons and present sensitivity estimates for SND@LHC, comparing them with existing bounds from several experiments operating at different energy scales.

II. Dirac Dark States and the Dipolar Model

In our search for dark sector phenomena, fermionic dark states have been one of our candidates in a number of studies. An effective field theory approach to Dirac dark matter, similar to what we have addressed here, has been conducted in [6] along with additional models arising from SUSY. A $U(1)_{B-L}$ extension of the Standard Model has been studied in [7] where the dark state χ couples to the gauge boson Z' . In [8], a singlet model of Dirac dark matter has been studied where the Standard Model has been extended by two chiral fermions ψ_L and ψ_R that form the Dirac dark matter ψ followed by a real scalar field ϕ .

Our work focuses on a neutral dark state carrying an electric or magnetic dipole moment. Such a state is naturally a fermion and we treat it as a Dirac particle. Majorana particles have vanishing electric and magnetic dipole moments which restrict our choice of states. In the context of dark matter, we know the coupling to photons should be small enough to keep dark matter “dark”. Current experimental limits reduce the viable parameter space substantially; hence, suppressing the coupling over the mass scale we have considered. A detailed analysis on the theory of dipolar dark matter has been addressed in [9].

In this work, we adopt a dipole model of a viable dark matter candidate that interacts with the SM via magnetic and electric dipole moment operators as described in eqn.(1). This model will be utilized in a proficient imposition of constraints. It will also aid us in looking at dark states in the MeV scale by focusing on decays of unflavored mesons. In the higher-mass regime, the Drell-Yan channel overwhelmingly dominates, suppressing the contributions from other processes.

The Dirac dark sector couples to SM through dimension-5 electric and magnetic dipole moment operators under the Minimal Flavor hypothesis as described in [10] in the form of a doublet and a triplet. The possible Higgs and Z boson interactions are heavily constrained and are irrelevant to our analysis. For efficient imposition of constraints and simplification

of the resulting phenomenology, we consider a singlet model in this work as shown below:

$$\mathcal{L} = \frac{c_A^{MDM}}{\Lambda} \bar{\chi} \sigma_{\mu\nu} \chi_R F^{\mu\nu} + i \frac{c_A^{EDM}}{\Lambda} \bar{\chi} \sigma_{\mu\nu} \gamma_5 \chi_R F^{\mu\nu} \quad (1)$$

There have been prior studies that look into such higher dimensional interactions mediated by the photon. Signatures of Dirac dark matter at direct detection experiments through interactions induced by electromagnetic form factors have been analyzed through a formalism that relates the signal rate to the form factors that includes electric and magnetic dipole moments in [11]. A possible UV completion model of dimension-5 and 6 have been discussed in the previously mentioned reference as well. Constraints on electromagnetic dipole interactions, including direct dipole moments for Dirac fermions as well as transition dipole moments relevant for Majorana fermions, have been studied in [12] in relation to several nuclear recoil experiments.

III. The Scattering and Neutrino Detector

The Scattering and Neutrino Detector(SND) is a newly found facility at the LHC that has been designed to detect neutrinos of all three flavors and aims to take measurements of neutrinos in an untapped parameter space. Located 480 m away from the ATLAS IP in the TI18 tunnel, and positioned slightly off-axis covering the pseudorapidity range of $7.2 < \eta < 8.4$, it aims to study neutrinos originating mostly from charmed hadron decays. SND@LHC is expected to be sensitive in measuring scatterings of Feebly Interacting Particles(FIPs) in its target. A schematic diagram of the detector has been provided in Fig.(1).

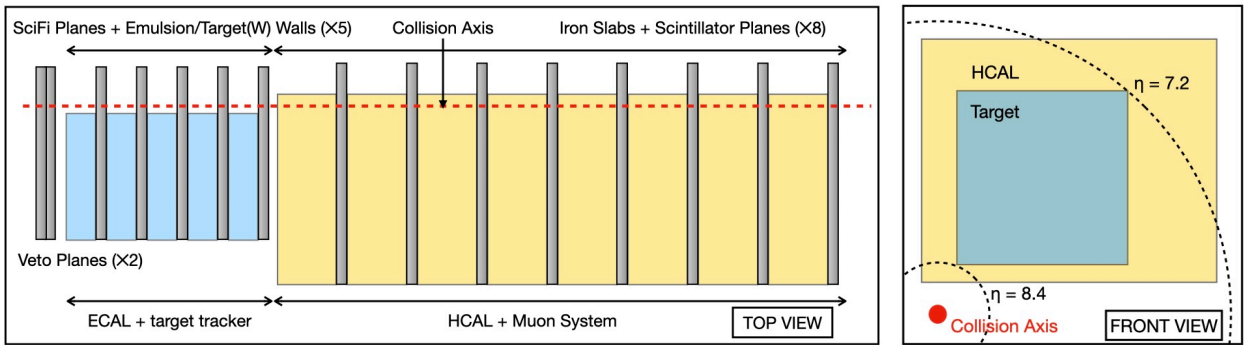


FIG. 1. **Left:** Schematic layout of the SND@LHC from a top view. **Right:** Frontal view of the target and HCAL with the collision axis.

A. Structure of SND@LHC

A detailed description of the working and assembly of the detector components can be found in [13] and [14]. The veto system detects charged particles by scintillation. In our analysis, we consider the target and vertex detector to register signals from the dark sector interacting with the tungsten target. The target system comprises five 40×40 cm² bricks of emulsion cloud chambers (ECC) alternated with Scintillating fiber (SciFi) plates. Each emulsion plate contains 60 emulsion films with 59 1mm thick tungsten plates alternately positioned between the films. The ECCs facilitate micrometric accuracy of any charged particle tracks and reconstruct interactions of neutrinos and other events that occur within an emulsion brick. The scintillating fiber plates are designed to measure energies of electromagnetic and hadronic showers with a spatial and temporal resolution of 50 μm and 100 ps respectively. The muon system consists of eight scintillating planes interleaved between 20 cm thick iron slabs. It will identify muon neutrinos and hence, muon neutrino charged current interactions [15]. Combined with the SciFi planes, it will measure energies of hadronic showers.

B. How sensitive is the SND@LHC?

Sensitivity projections for dark sector scenarios relevant to SND@LHC have been investigated in prior works and hence, providing quantitative reach estimates in the relevant parameter spaces. The sensitivity of the SND@LHC in probing leptophobic dark matter coupled to quarks via a vector mediator has been studied in [15]. Detection prospects of complex scalar and Majorana fermionic dark matter have been analyzed in [16] within the framework of far-forward detectors including SND@LHC. A model describing long lived light dark photon has been systematically studied in [17] addressing detection at SND@LHC.

We will study a model where a possible Dirac dark matter candidate couples to SM via dimension-5 dipole interactions mediated by the SM photon. The sensitivity curve corresponding to this model will comprise setting a lower bound to couplings in order to register signals in our detector.

C. Neutrino Background

The scattering of FIPs off protons is mimicked by neutral current (NC) neutrino scattering events. The background is partly contributed by inelastic scattering of neutrinos on protons

through neutral-current(NC) scattering. In [14], the neutrino background was simulated using the offline software framework **snndsw**, that was developed by the SHiP [18] collaboration by utilizing the **FairRoot** [19] framework. **snndsw** integrates several high-energy physics software packages that allow a detailed simulation of detector signals and backgrounds. Across all flavors, the number of NC scattering events is found to be 450 upon normalization to an integrate luminosity of 150 fb^{-1} . In [13], the neutrino interactions have been simulated using **Genie** [20] which results in 550 NC interactions at the SND@LHC target. Charged current interactions have also been discussed in above referred works but are irrelevant to our study.

For elastic scattering, the number of single track events during the entire time of operation is 1.7 [15]. In the case of elastic scattering off electrons, the background largely comes from ν_e scattering on electrons and can be ignored safely. Neutrinos scattering on electrons has been widely studied in [21–24]. The contributions of both these elastic processes to the background can be eliminated by a selective analysis of topology and kinematics.

SND@LHC can utilize its time of resolution which is of $\sim 200\text{ps}$ to perform model-independent searches for FIPs by combining a recoil signature with a time of flight measurement to suppress the background comprising neutrino interactions. It is expected that SND@LHC will be able to resolve scattering signals of massive FIPs from neutrino scattering events in certain regions of a parameter space spanned by the momentum and mass of the FIP as discussed in [14]. However, the average energy of FIPs corresponding to our model is too large to belong within the region of the parameter space in which such a search for FIP can be performed. Hence, detection by time of flight measurement is not applicable in the detection of our model described in eqn.(1).

IV. Production Channels of Dark Sector

All relevant direct production channels of dark state(χ) as shown in Table(I), have been simulated on **MadGraph5_aMC@NLO** [25] after the model was implemented through **FeynRules** [26]. Meson decays have been analyzed using **FORESEE** [27]. The projections have been computed for integrated luminosities of 250 fb^{-1} and 3000 fb^{-1} corresponding to SND@LHC collections during the Run-3 and Run-4 of the LHC. All production channels have been listed in Table(I).

Production Channel	Feynman Diagram
Drell-Yan: $q \bar{q} \rightarrow \gamma^* \rightarrow \chi \bar{\chi}$	
Bremsstrahlung: $q q \rightarrow q q \gamma^* ; \gamma^* \rightarrow \chi \bar{\chi}$	
Mono-Jet: $q g \rightarrow q \gamma^* ; \gamma^* \rightarrow \chi \bar{\chi}$	
Pseudoscalar Meson Decay: $P \rightarrow \gamma^* \gamma ; \gamma^* \rightarrow \chi \bar{\chi}$	
Vector Meson Decay: $V \rightarrow \gamma^* \rightarrow \chi \bar{\chi}$	

TABLE I. Production channels of χ and $\bar{\chi}$. Significant and considered channels have been shown in shaded cells. For bremsstrahlung and mono-jet processes, one of several diagrams has been shown. The two processes are sub-leading in comparison to the Drell-Yan and numerically insignificant.

A. Drell-Yan process

For masses beyond 1 GeV, we have used `MadGraph5_aMC@NLO` [25] to find the cross-sections of Drell-Yan process and used `MadAnalysis 5` [28] to find the number of dark states propagating towards the SND@LHC target. Contributions from mono-jet and bremsstrahlung are substantially weaker and are safe to ignore. The obtained results presented in Fig.(2), will be later used in the following sections to obtain the projection of the detector.

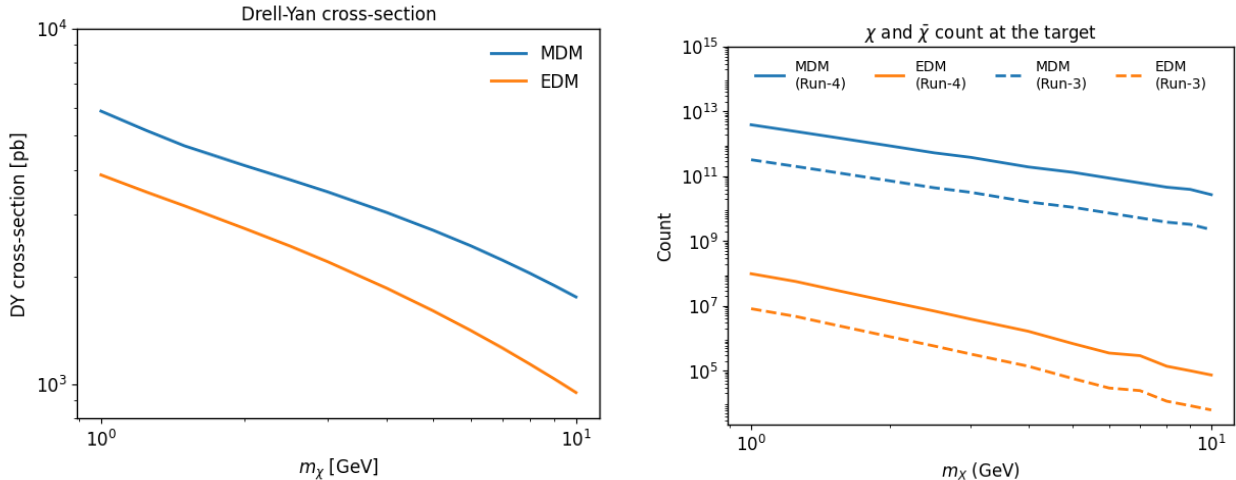


FIG. 2. **Left:** Drell-Yan production cross-section for coupling set to 1 GeV^{-1} . **Right:** Incident χ and $\bar{\chi}$ at SND@LHC target for coupling set to 1 GeV^{-1} . The count has been normalized to both the Run-3 (250 fb^{-1}) and Run-4 (3000 fb^{-1}) data accumulation.

B. Decay of Unflavored Mesons

In the lighter-mass sector, specifically below 1 GeV, we resort to meson decays as the source of dark state production. Heavier mesons such as $\Upsilon(nS)$ and J/Ψ allow us to dive into a segment of the mass region ($\lesssim 5 \text{ GeV}$) of the Drell-Yan process. In this subsection, we investigate meson decays and impose constraints based on the invisible width of the mesons. We assume the entire invisible width is available for decays into dark state pairs.

1. Meson Decay Widths

We calculate the decay widths and branching ratios of mesons into $\chi\bar{\chi}$ pairs according to the model (1) as mentioned in [29] with individual treatment of MDM and EDM components. We then proceed to constrain the resulting values with the invisible branching fractions as

presented in [30].

The branching ratio of the vector mesons(V) into $\chi\bar{\chi}$ pairs can be computed from,

$$BR(V \rightarrow \chi\bar{\chi}) = BR(V \rightarrow e^-e^+) \frac{f_\chi(m_V^2)}{f_e(m_V^2)} \sqrt{\frac{m_V^2 - 4m_\chi^2}{m_V^2 - 4m_e^2}} \quad (2)$$

The decay width of pseudoscalar mesons (P) can be calculated from,

$$\Gamma_\chi = \int_{4m_\chi^2}^{m_P^2} ds_{\chi\bar{\chi}} \Gamma_{P \rightarrow \gamma\gamma^*(s_{\chi\bar{\chi}})} \frac{f_\chi(s_{\chi\bar{\chi}})}{16\pi^2 s_{\chi\bar{\chi}}^2} \sqrt{1 - \frac{4m_\chi^2}{s_{\chi\bar{\chi}}}} \quad (3)$$

where $s_{\chi\bar{\chi}}$ is the invariant mass squared of the $\chi\bar{\chi}$ pair and $\Gamma_{P \rightarrow \gamma\gamma^*}$ is the decay width of the pseudoscalar meson into a photon pair; with one photon being off-shell.

$$\Gamma_{P \rightarrow \gamma\gamma^*} = \frac{\alpha^2(m_P^2 - s_{\chi\bar{\chi}})^3}{32\pi^3 m_P^3 F_P^2} \quad (4)$$

where F_P is the decay constant of the meson and can be sourced from [31],[32] and [33]. The functions f_χ and f_e are stated below:

$$MDM : f_\chi(s_{\chi\bar{\chi}}) = \frac{8}{3}(c_A^{MDM})^2 s_{\chi\bar{\chi}}^2 \left(1 + \frac{8m_\chi^2}{s_{\chi\bar{\chi}}}\right) \quad (5)$$

$$EDM : f_\chi(s_{\chi\bar{\chi}}) = \frac{8}{3}(c_A^{EDM})^2 s_{\chi\bar{\chi}}^2 \left(1 - \frac{4m_\chi^2}{s_{\chi\bar{\chi}}}\right) \quad (6)$$

$$f_e(m_V^2) = \frac{16\pi\alpha}{3} m_V^2 \left(1 + \frac{2m_e^2}{m_V^2}\right) \quad (7)$$

2. Cross-Sections and Spectra

We employ **FORESEE** [27] to simulate the production of dark state χ from the decays of unflavored vector and pseudoscalar mesons. **FORESEE** is a package that enables us to simulate different production and decay modes of BSM states when pre-defined interactions along with geometric cuts specific to a detector are applied by the user. It also includes spectra of several mesons generated through the appropriate event generators in the forward region. **FORESEE** also allows us to simulate over different collision energies and have a choice of generator for certain mesons.

We have shown a couple of examples of meson spectra obtained in Fig. (3). The spectra of lighter mesons($\omega, \rho, \phi, \eta, \eta', \pi^0$) have been obtained through the **EPOS LHC** [34] generator

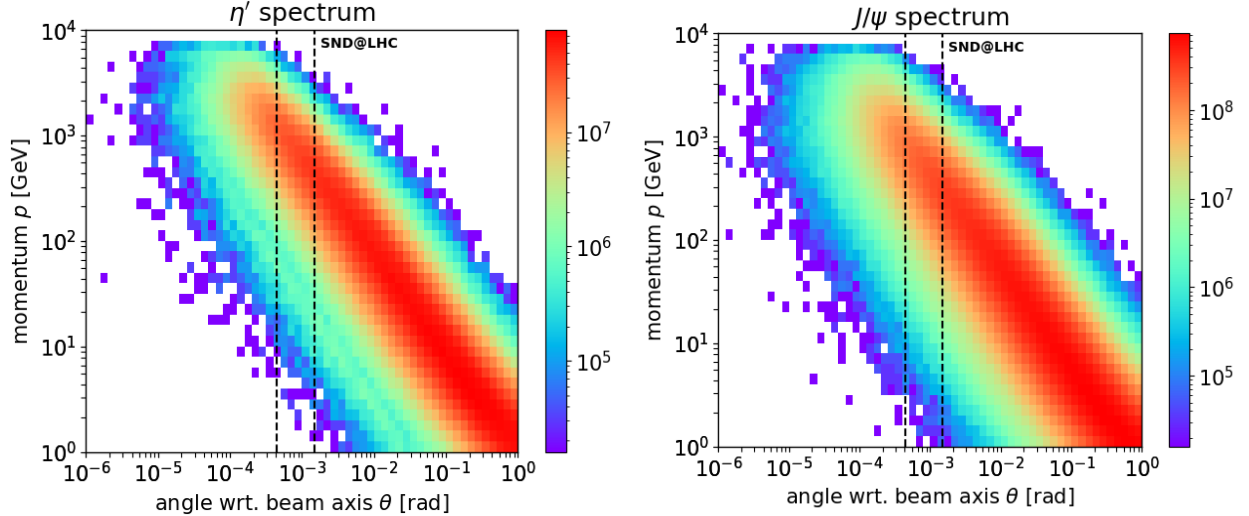


FIG. 3. **Left:** η' spectrum using EPOS LHC generator. **Right:** J/ψ spectrum using Pythia 8 generator. The range of polar angles corresponding to SND@LHC geometric acceptance has been shown with two black dotted lines. The color map represents the cross-section in pb per bin on a logarithmic scale.

implemented in the CRMC [35] interface, while heavier mesons ($J/\psi, \Psi(2S), \Upsilon(nS)$) have been generated through Pythia 8 [36] and tuned to LHCb [37–39] data.

Our following study has been conducted by treating the electric and dipole moments individually. Eqn.(2) has been used to input the branching ratio of the vector mesons. We can apply the differential branching ratios [40] of pseudoscalar mesons to simulate the 3-body decays into $\gamma\chi\bar{\chi}$.

$$\frac{dBR_{P \rightarrow \gamma\chi\bar{\chi}}^{(MDM)}}{dq^2 d(\cos\theta)} = BR_{P \rightarrow \gamma\gamma} \left[\frac{(c_A^{MDM})^2}{4\pi^2} \left(1 - \frac{q^2}{M^2} \right) \sqrt{1 - \frac{4m_\chi^2}{q^2}} \left(\frac{8m_\chi^2}{q^2} + \left[1 - \frac{4m_\chi^2}{q^2} \right] \sin^2\theta \right) \right] \quad (8)$$

$$\frac{dBR_{P \rightarrow \gamma\chi\bar{\chi}}^{(EDM)}}{dq^2 d\cos\theta} = BR_{P \rightarrow \gamma\gamma} \left[\frac{(c_A^{EDM})^2}{4\pi^2} \left(1 - \frac{q^2}{M^2} \right) \sqrt{1 - \frac{4m_\chi^2}{q^2}} \left(1 - \frac{4m_\chi^2}{q^2} \sin^2\theta \right) \right] \quad (9)$$

In the analysis that follows, we have fixed our coupling to 1 GeV^{-1} . The $\chi\bar{\chi}$ pair production cross-section from decays of mesons has been obtained through a p-p collision at 14 TeV for unit coupling and shown in Fig.(4). In our analysis, we have considered the unflavored mesons available in FORESEE. In the cross-sections computed above, we have treated magnetic and electric dipole moments separately. MDM and EDM cross-sections

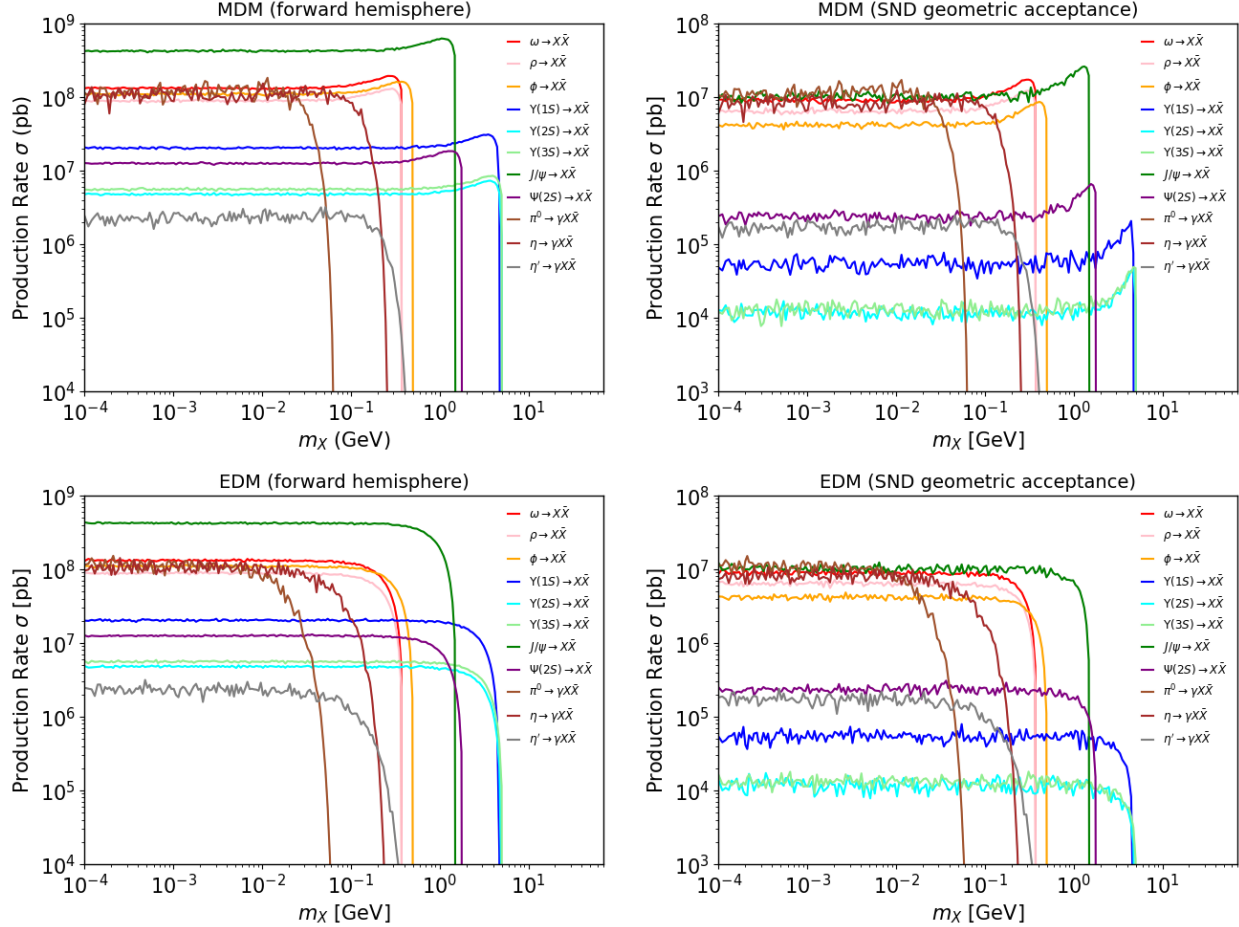


FIG. 4. We present here the $\chi\bar{\chi}$ pair production cross-section both in the half hemisphere and the annular region described by the pseudorapidity coverage of SND@LHC. **Top Left and Top Right:** MDM cross-section in forward hemisphere and within $7.2 < \eta < 8.4$. **Bottom Left and Bottom Right:** EDM cross-section in forward hemisphere and within $7.2 < \eta < 8.4$.

behave similarly in low mass limit and start differing near threshold masses. A similar model-independent analysis has been conducted in Appendix C for similar decay channels. As expected, the cross-sections approach zero when m_χ equals half the mass of the decaying meson. The ratio of combined incident χ and $\bar{\chi}$ in the region spanned by η and ϕ cuts for SND@LHC to the area within $7.2 < \eta < 8.4$ is 0.176.

A momentum spectrum has been obtained for dark states after having defined the dynamics of our model in Fig.(5). In direct detection experiments, the dark state spectrum is significant in determining the recoil energy spectrum at the target of the detector. The DM spectra can help distinguish different models, which might be searched for at the facility. In

addition, the spectra can help us optimize the structure of the detectors that would be used to probe these models.

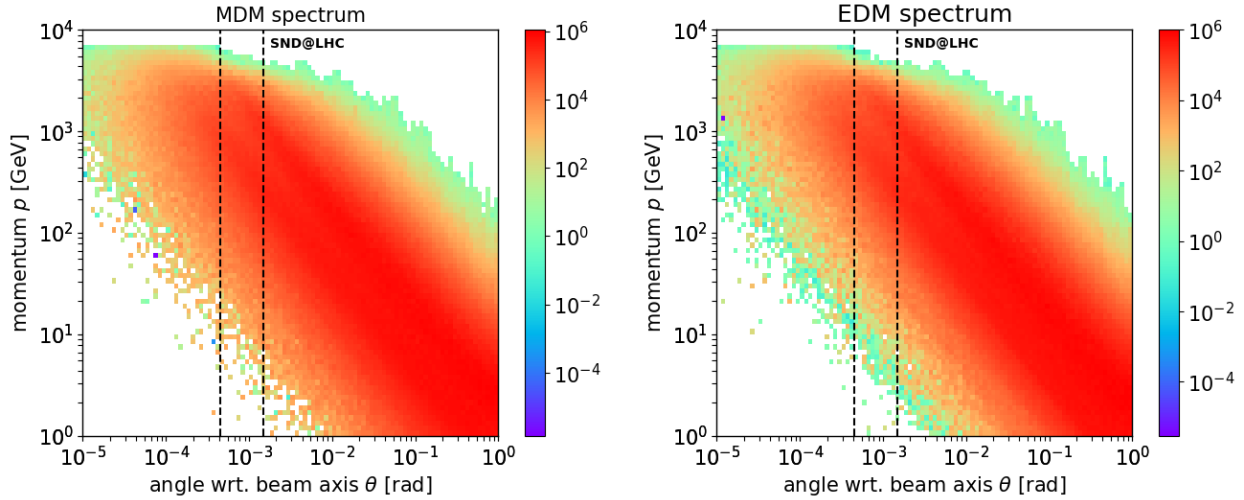


FIG. 5. Spectrum for $m_\chi = 0.1$ GeV with coupling set to 1 GeV^{-1} . **Left:** MDM; **Right:** EDM. The range of polar angles corresponding to SND@LHC geometric acceptance has been shown with two black dotted lines. The color map represents the cross-section in pb per bin on a logarithmic scale.

A distinct spectrum corresponding to different production channels has also been shown in Fig.(6) for a Monte Carlo sampling of 100. Such momentum spectra tell us the expected recoil energies at the target when considering specific resonance channels. The approximate similarity of spectra obtained in Fig.(6) can be traced back to Fig.(5) that shows minimal difference as well.

V. Sensitivity of SND@LHC

The sensitivity of SND@LHC in the detection of scalar dark matter has already been investigated in [15]. It also discusses the sensitivity of the detector in probing decays of dark scalars, dark photons and heavy neutral leptons. We have aimed at calculating the limits on the detection of our current model containing a potential dark matter via scattering on electrons at the target assuming unit efficiency of detection.

An efficient way to impose a limit on the coupling comes from studying the invisible decay widths of mesons. The condition that our model has to produce $\chi\bar{\chi}$ pairs within

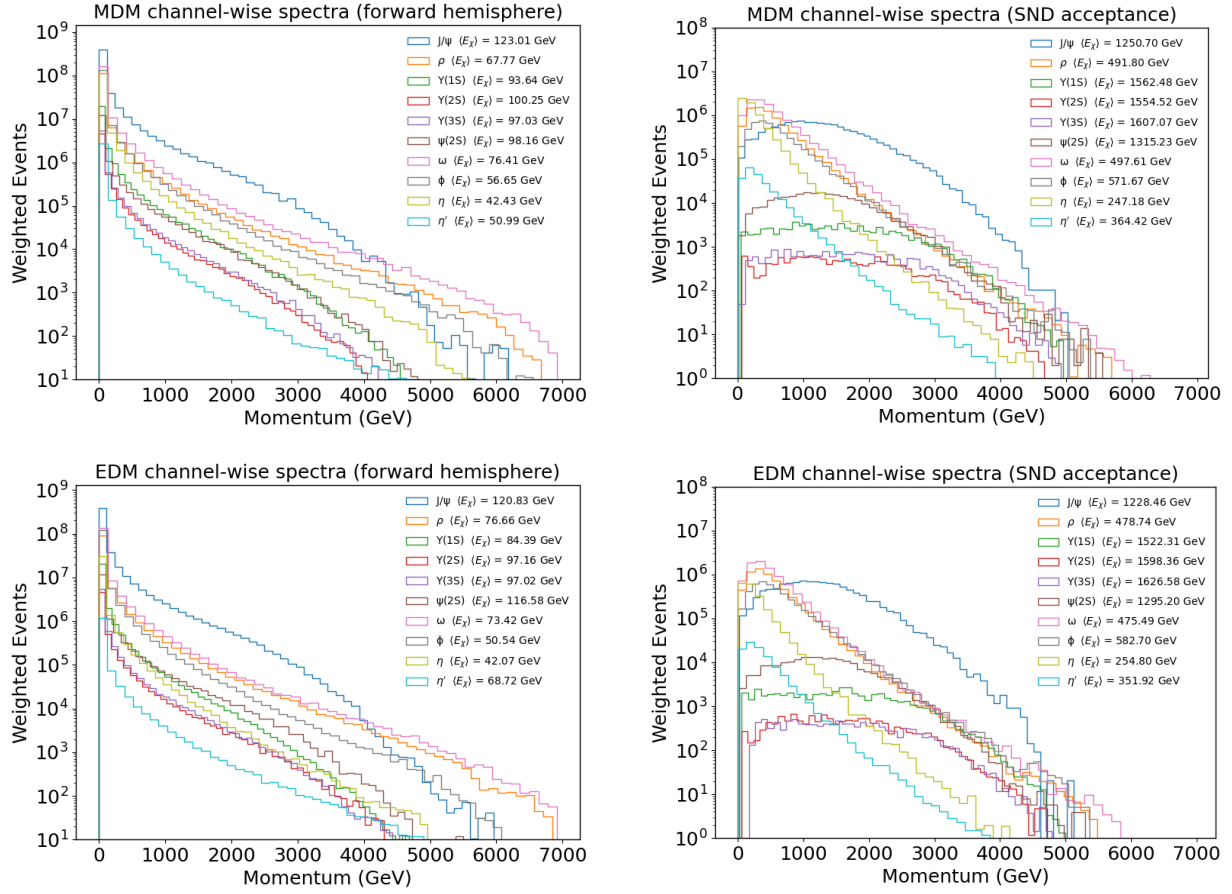


FIG. 6. Weighted events as a function of momentum for $m_\chi = 0.1$ GeV for different channels of production. a) MDM spectrum in the forward hemisphere. b) MDM spectrum within $7.2 < \eta < 8.4$. c) EDM spectrum in the forward hemisphere. d) EDM spectrum within $7.2 < \eta < 8.4$. Along with the histograms we also mention the average momenta of χ produced from each meson decay for both situations. The data have been acquired with the coupling set to 1 GeV^{-1} .

the allowed invisible decay widths of each meson, allows us to put an upper bound on the allowed couplings as illustrated in Fig.(7). We consider decays of mesons for which we have an experimental record of their invisible branching ratios. The bounds placed by $\Upsilon(1S)$ are by far the most stringent. Future improvements in the experimental measurements of invisible branching ratios will affect our limits.

[41] also addresses bounds placed by rare meson decays such as $K^+ \rightarrow \pi^+ \chi \bar{\chi}$ and $B^+ \rightarrow K^+ \chi \bar{\chi}$. The K^+ decay constraints c_A^{MDM} or $c_A^{EDM} \lesssim 1.5 \times 10^{-4} \mu_B$ in certain momentum ranges when the mass of χ is in the MeV scale while the B^+ decay puts the constraint c_A^{MDM} or $c_A^{EDM} \lesssim 3 \times 10^{-3} \mu_B$, where μ_B is the Bohr magneton.

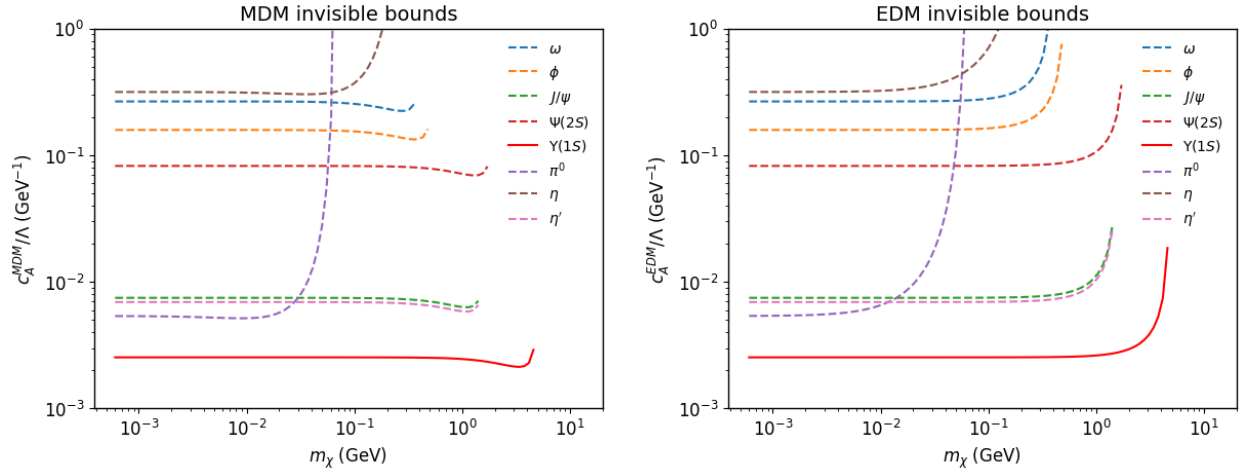


FIG. 7. Bounds derived from inv. B.R. of decaying mesons. **Left:** MDM. **Right:** EDM

An essential part of obtaining the projection of a detector includes the energies and the population of the χ or $\bar{\chi}$ population incident on the target. We take into account both direct detection and meson decays as sources of $\chi/\bar{\chi}$ production and project the average energies and population for unit coupling as functions of m_χ as shown in Fig.(8). The variation of $\langle E_\chi \rangle$ can be related to the production cross-section from different channels and their spectra for a particular mass. The energy plot shows dips at points where the mass exceeds the kinematic limits of specific mesons. For example, at $m_\chi \sim 1.5$ GeV, the J/ψ channel becomes kinematically forbidden and the energy sees a dip because J/ψ exhibits higher weighted events compared to other mesons over a significant region of the momentum-region. Although Drell-Yan process allows the produced $\chi\bar{\chi}$ pairs to attain higher energies, the plot sees a dip at $m_\chi \sim 4.7$ GeV for the kinematic limits corresponding to $\Upsilon(nS)$ mesons are crossed. The energy keeps increasing beyond that point because Drell-Yan produces heavier particles with larger momenta.

In the dark state population plot, the contribution from meson decays and Drell-Yan has been added. We see a dip at $m_\chi \sim 1.5$ GeV because the decay channel of J/ψ becomes inaccessible kinematically. The contribution from meson decays drops to zero after $m_\chi \sim 4.7$ GeV when the $\Upsilon(nS)$ channels become kinematically forbidden. The overlap of Drell-Yan contribution masks the clear dips in meson decay contribution. Beyond $m_\chi \approx 4.7$ GeV, Drell-Yan dominates the curve for both interactions.

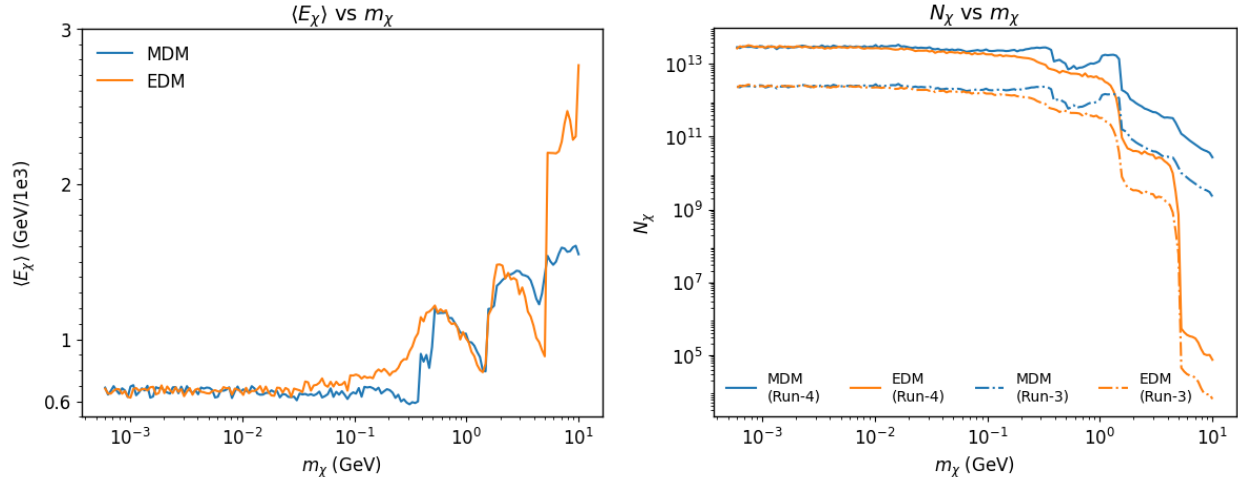


FIG. 8. **Left:** Average energy $\langle E_\chi \rangle$ in SND@LHC acceptance varied with mass. The average has been computed over all channels for each specific value of m_χ . **Right:** χ and $\bar{\chi}$ populations at the target of SND@LHC. The populations have been normalized to both the Run-3 (250 fb^{-1}) and Run-4 (3000 fb^{-1}) data accumulations. In both plots, we have considered all relevant channels of production.

A. χN scattering

Several experiments probing DM-nucleus scattering have been conducted producing limits on the corresponding cross-section. Direct detection experiments looking into DM-nucleus cross-sections in the mass range of few GeV to several TeV have significantly constrained the parameter space. Experiments like LUX [42], PandaX-II [43], XENON1T [44], DarkSide-50 [45], CDMSlite [46], CDEX-0 [47], CDEX-1 [48–51], CDEX-10 [52, 53], CDEX-1B [54, 55] probe the GeV scale and beyond. In the sub-GeV region, which is of interest to us, experiments like CRESST-III, XQC, CDEX-1B and CDEX-10 [56–58] have placed constraints. However, such experiments enforce limits on the per-nucleon cross-section which is translated to DM-nucleus cross-section under the assumption that the interaction mediating the scattering is momentum-independent. This underlying condition of drafting the cross-section limits forbids us from deriving constraints on both MDM and EDM interactions.

When considering scattering on nuclei, we need to take into account the momentum dependence of both MDM and EDM interactions. The different dependence on recoil energies has been explicitly stated in Appendix A. This necessitates the presence of MDM and EDM scattering cross-section limits from other experiments in order to draw a comparison of χN

sensitivity of SND@LHC with other experiments. The χN elastic and deep inelastic scattering cross-sections for both interactions with $c/\Lambda = 1 \text{ GeV}^{-1}$ are $\sim 9.48 \times 10^{-31} \text{ cm}^2$ and $4 \times 10^{-29} \text{ cm}^2$ respectively and can be used as benchmark points for comparison with other χN scattering experiments.

B. χe scattering

Several direct detection experiments have probed elastic scattering on electrons in a wide mass region from 10s of keV to several GeV. Constraints from these experiments such as these allow us to compare the prospects of our model at SND@LHC. Direct detection experiments with semiconductor targets [59–63], noble liquid-based detectors [64–68] have provided limits on DM-electron elastic scattering cross-sections. Some EDM constraints corresponding to protoSENSEI@MINOS and CDMS-HVeV have been obtained from [69, 70]. [71] presents a list of DM-electron cross-section limits that have been mentioned here as well.

Halo dark matter with a mass around 10 MeV has a kinetic energy of about 5 eV which can be amplified by scattering off electrons in the Sun and being reflected towards the Earth with an energy in the keV range [72]. This allows us to probe lighter dark matter more efficiently compared to halo origins. We adopt constraints derived from solar reflected dark matter(SRDM) derived from XENON1T [72–75] in the low mass region that we are interested in.

DM-electron cross-sections are expressed in terms of a reference cross-section defined as [76]:

$$\bar{\sigma}_e = \frac{1}{16\pi(m_e + m_\chi)^2} \overline{|\mathcal{M}_{\chi e}|^2}_{q^2 = \alpha^2 m_e^2} \quad (10)$$

where,

$$\overline{|\mathcal{M}_{\chi e}(q)|^2} = \overline{|\mathcal{M}_{\chi e}(q_0)|^2}_{q_0^2 = \alpha^2 m_e^2} \times |F_{DM}(q)|^2 \quad (11)$$

We are considering the squared amplitudes for scattering of DM off free electrons after averaging over initial states and summing over final states. The leading terms of the amplitudes $|\mathcal{M}_{\chi e}|^2$ are laid down below:

$$\text{MDM: } 64\pi \frac{c_A^{MDM^2}}{\Lambda^2} \alpha m_\chi^2 \quad (12)$$

$$\text{EDM: } \frac{256\pi c_A^{EDM^2} \alpha m_e^2 m_\chi^2}{q^2 \Lambda^2} \quad (13)$$

Hence, $F_{DM} = 1$ for MDM and $\alpha m_e/q$ for EDM. We explore the limits on $\bar{\sigma}_e$ that feature

the same form factors. Experimental limits on χe cross-section have been established by several direct detection experiments and have been shown in Fig.(9).

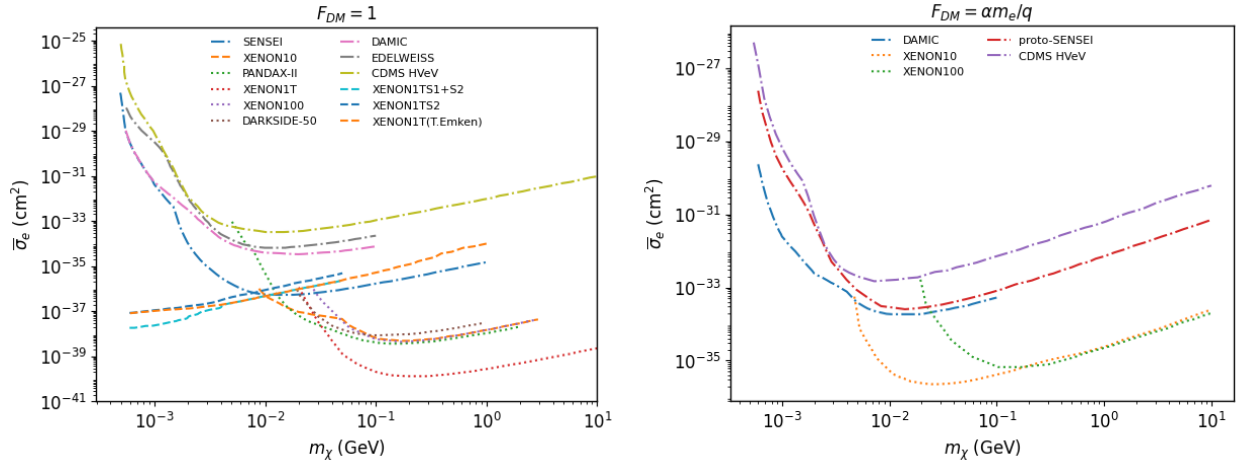


FIG. 9. Upper limits on χe reference cross-section $\bar{\sigma}_e$ corresponding to 90% C.L. **Left:** Upper limits on cross-sections corresponding to form factor $F_{DM} = 1$. **Right:** Upper limits on cross-sections corresponding to form factor $F_{DM} = \alpha m_e/q$.

Applying the projected dynamics of χ shown at the start of this section, we have produced a sensitivity curve for SND@LHC that can be put against current direct detection limits as shown in Fig.(10). We have obtained the sensitivity line corresponding to background-free ‘one- χ ’ or 2.3 events for MDM and EDM separately. In the projected limits, we observe that the curve strongly depends on the DM population for the variation in χe cross-section is too small to be significant.

The constraints from direct detection experiments are derived at energies $\sim \mathcal{O}(\text{keV})$, while SND@LHC operates at several hundreds of GeV to a few TeV. In order to obtain a fair comparison, we evolve the low energy constraints via the appropriate RGE equations as shown in Appendix B. However, the change in constraints is insignificant when considering the RGE evolution of dimension-5 MDM and EDM operators. MDM and EDM, being CP-even and CP-odd respectively, do not mix with each other, and the evolution is entirely governed by the running of SM parameters.

We also present our sensitivity plot along with constraints provided by beam-dump, fixed-target, and electron-positron collider experiments in Fig.(11). Experiments such as LEP [41], BaBar [77], CHARM II [78], E613 [79], LSND [80], and MiniBooNE [81, 82]

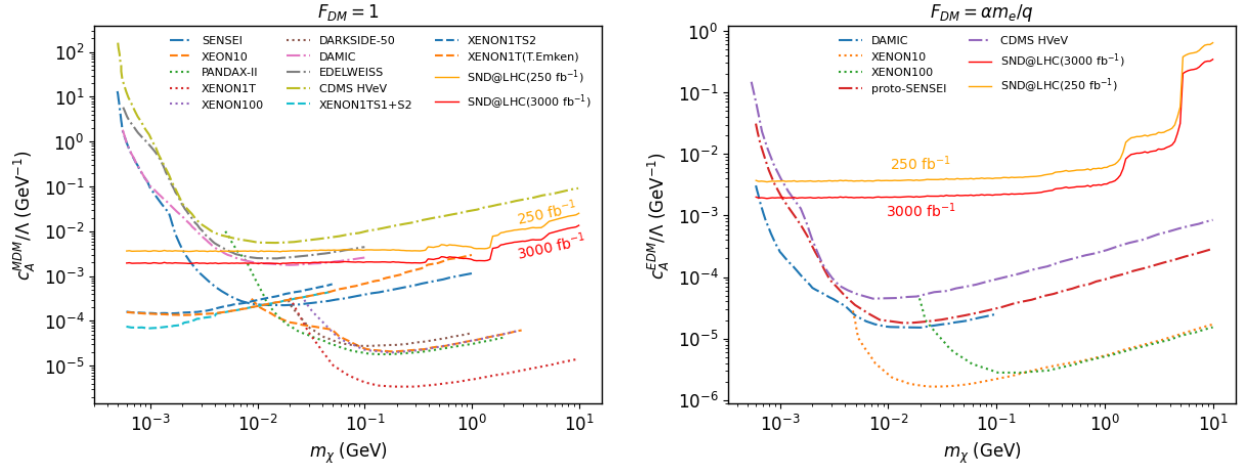


FIG. 10. Projected sensitivity plot of SND@LHC shown against: (Left) 90% C.L. constraints on MDM couplings fixed by DD experiments ($F_{DM}=1$). (Right) 90% C.L. constraints on EDM couplings fixed by DD experiments ($F_{DM} = \alpha m_e/q$). Sensitivity reaches of SND@LHC corresponding to both the Run-3 (250 fb^{-1}) and Run-4 (3000 fb^{-1}) have been shown.

have imposed bounds on both MDM and EDM bounds. A compilation of several such bounds has also been presented in [83]. The corresponding projections at future electron colliders have been studied in [84]. Since such experiments operate at much higher scale of transfer momentum, there is no requirement of applying the renormalization group equations for a valid comparison with projections at SND@LHC. Although there are indirect and cosmological constraints on the dipole moments as discussed in [41, 85, 86], we do not mention them in Fig.(10) and Fig.(11). Apart from experimental bounds, [40, 41] also looks into the generated relic abundance for both MDM and EDM interactions. Future upgraded versions [87–90] of SND@LHC are expected to have improved projections aimed at different dark sectors, including the Dirac dipole model.

We proceed to present the region of EFT validity for both MDM and EDM interactions in Fig.12. The EFT validity criterion has been chosen as $c/\Lambda < (10 q_{max})^{-1}$, where the factor of 10 is chosen to ensure a comfortable separation between the momentum transfer and the cut-off scale.

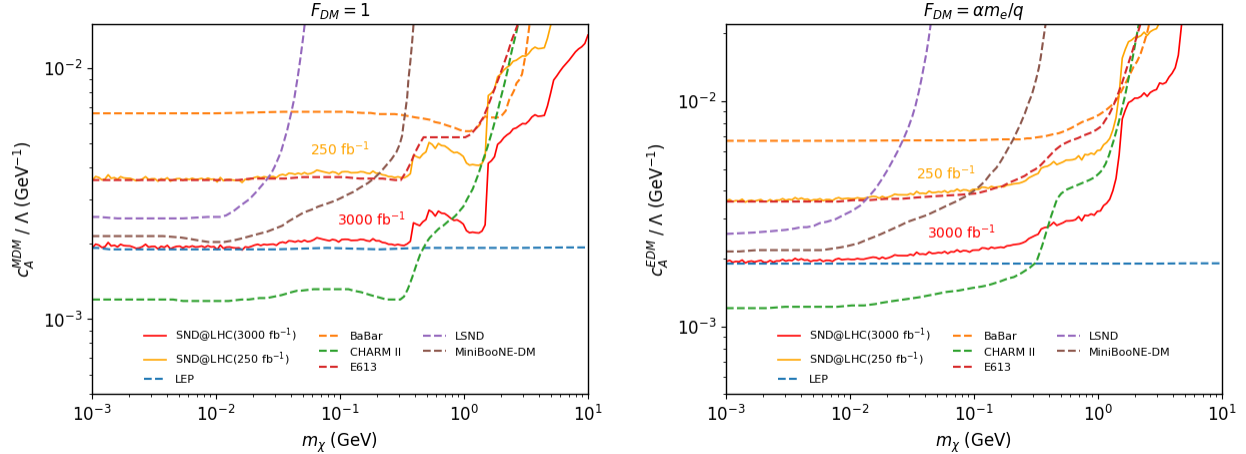


FIG. 11. Projected sensitivity plot of SND@LHC shown against constraints from beam-dump, fixed-target and e^-e^+ collider experiments. Left: 90% C.L. constraints on MDM couplings. Right: 90% C.L. constraints on EDM couplings. Sensitivity reaches of SND@LHC corresponding to both the Run-3 (250 fb^{-1}) and Run-4 (3000 fb^{-1}) have been shown.

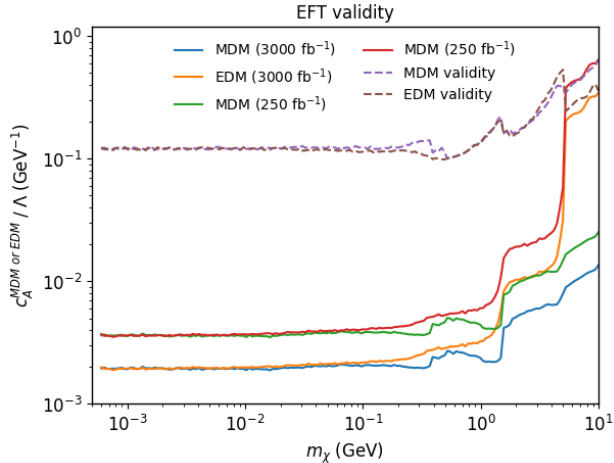


FIG. 12. EFT validity region of MDM and EDM sensitivities. In this figure, we have considered the projected reach corresponding to both 250 fb^{-1} and 3000 fb^{-1} .

VI. Conclusions and Outlook

We have analyzed the prospects for detecting fermionic dark states at SND@LHC in the benchmark scenario where the leading interaction with the Standard Model is described by electric and/or magnetic dipole operators. Propagating the resulting fluxes to the SND@LHC target, we evaluated the scattering signal rates for nuclei and electrons and

presented projected sensitivities for LHC integrated luminosities relevant to both the current and HL-LHC program.

Our results show that SND@LHC can probe dipole moments in regions that are complementary to existing experimental bounds comprising direct-detection, beam-dump, and collider searches, for sub-GeV to few-GeV dark matter. We have also studied the parameter space for which the effective dipole description remains self-consistent at the momentum transfers relevant for scattering at the target region. We identify the domains where the EFT remains applicable even with a strict validity condition imposed.

As seen from the comparison between the SND@LHC sensitivity and the existing direct detection constraints, solar reflected dark matter severely restricts the low-mass region of the MDM parameter space. However, SND@LHC in the HL-LHC era can probe the low-mass region more effectively than DAMIC around $m_\chi \sim 0.5$ MeV. Extending the sensitivity of SND@LHC to even lower masses allows access to regions of parameter space currently unconstrained by present direct detection experiments.

A comparison of the SND@LHC with beam-dump, fixed-target and e^-e^+ collider searches reveals that LEP and CHARM II currently provide the strongest limits to the Dirac Dipole model. Overcoming these bounds would require an enhancement of the incoming dark state flux at the SND@LHC target by approximately a factor of 5 to probe new parameter space at $\mathcal{O}(-1)$ GeV, while an enhancement by a factor of $\gtrsim 7$ would allow us access to an entirely new parameter space unconstrained by any present-day experiment. Such enhancements can be implemented by widening the target region or extending the scattering length in the detector. However the available space in the TI18 tunnel of the LHC can put practical restrictions on such modifications.

Acknowledgments

The author expresses his gratitude to Sudhir Kumar Vempati and Biplob Bhattacherjee for discussions and guidance and also for going through the manuscript. The author would also like to thank Aadarsh Singh for his initial assistance with software. The author acknowledges financial support from Ministry of Human Resource Development, Government of India, via Prime Minister Research Fellowship (PMRF).

A. Relativistic Elastic Cross-Section

In a relativistic treatment, the recoil differential elastic cross-section for a nucleus with charge Z , electric and magnetic form factors F_E and F_M , mass m_N and spin I_N when scattering on a fermion χ with mass m_χ and energy E_χ , assumes the form [41]:

$$\frac{d\sigma}{dE_R} = \frac{1}{A} \left[g_E(E_R) \alpha Z^2 F_E^2(t) + g_M(E_R) \frac{\mu_N^2 m_N^2}{\pi} \frac{I_N + 1}{3I_N} F_M^2(t) \right] \quad (\text{A1})$$

where $A = (E_\chi^2 - m_\chi^2)(2m_N + E_R)$ and $t = 2m_N E_R$. The functions $g_E(E_R)$ and $g_M(E_R)$ are model-specific and given by:

$$\begin{aligned} \text{MDM: } \frac{g_E}{4(c_A^{MDM})^2} &= \frac{m_N}{2E_R} (4E_\chi^2 - 4m_\chi^2 + E_R^2) - (m_\chi^2 + 2m_N E_\chi) \\ \frac{g_M}{4(c_A^{MDM})^2} &= \frac{E_R}{2m_N} (m_\chi^2 - m_N^2 - 2m_N E_\chi) + (E_\chi^2 + m_\chi^2) \end{aligned} \quad (\text{A2})$$

$$\begin{aligned} \text{EDM: } \frac{g_E}{4(c_A^{EDM})^2} &= \frac{m_N}{2E_R} (E_R - 2E_\chi)^2 \\ \frac{g_M}{4(c_A^{EDM})^2} &= -\frac{E_R}{2m_N} (m_\chi^2 + m_N^2 + 2m_N E_\chi) + (E_\chi^2 - m_\chi^2) \end{aligned} \quad (\text{A3})$$

In case of scattering off nuclei with charge Z , the electric form factor is given by,

$$F_E(t) = \frac{Z a^2(Z) t}{(1 + a^2(Z) t)(1 + t/d(A))} \quad (\text{A4})$$

where, A is the mass number, $a(Z) = \frac{111Z^{1/3}}{m_e}$ and $d(A) = 0.164A^{-2/3}$. For heavy targets like tungsten, we neglect the magnetic form factor. In case of scattering off free electrons, we set $F_E = F_M = 1$, $Z = 1$, $I_N = \frac{1}{2}$ and $\mu_N = \mu_B$. m_i being the mass of the scattered target particle, the upper limit of integration in eqn.(A1) is given by,

$$E_R^{max} = \frac{2m_i(E_\chi^2 - m_\chi^2)}{m_i(2E_\chi + m_i) + m_\chi^2} \quad (\text{A5})$$

B. Renormalization Group Running

The Wilson coefficients are derived at very low energies $\sim \mathcal{O}(\text{keV})$ and have to be evolved to a higher energy scale \sim few hundred GeV to 1 TeV. The renormalization evolution of the Wilson coefficients is governed by the anomalous dimension matrix γ as described in [91]:

$$\frac{d\vec{C}(\mu)}{\ln \mu} = \gamma^T \vec{C}(\mu) \quad (\text{B1})$$

where, $\vec{C}(\mu)$ is the column of Wilson coefficients appearing in the renormalization group equation. However, MDM and EDM operators, being CP-even and CP-odd respectively, do not mix into each other and evolve independently. In order to keep the anomalous dimension matrices free of gauge couplings, we rescale our Wilson coefficients by $\alpha_1/2\pi$, where $\alpha_1 = g_1^2/4\pi$, g_1 being the $U(1)_Y$ coupling. Without the presence of any other CP-even or CP-odd operators, the evolutions of c_A^{MDM} and c_A^{EDM} are dictated by only the $\gamma(1,1)$ element. We will treat the anomalous dimension matrices as corresponding to an electroweak singlet. Since the evolution of both c_A^{MDM} and c_A^{EDM} are given by the same matrix, we will denote the coefficients as just c . Proceeding from eqn.(B1), with the above mentioned criteria, we arrive at,

$$\frac{1}{2} \frac{d(\alpha_1 c)}{d \ln \mu} = \frac{1}{2} \frac{\alpha_1}{4\pi} \frac{41}{3} \alpha_1 c \quad (B2)$$

The evolution of the $U(1)_Y$ coupling is given by,

$$\frac{dg_1}{d \ln \mu} = \frac{1}{16\pi^2} \frac{41}{6} g_1^3 \quad (B3)$$

Substituting eqn.(B3) in eqn.(B2), we conclude that c does not evolve in the absence of other operators with same CP characteristics. Hence,

$$\frac{dc}{d \ln \mu} = 0 \quad (B4)$$

The operator basis mentioned in [91] can be broken down to extract the interaction with the photon as follows:

$$\begin{aligned} \mathcal{Q}_1^{(5)} &= \frac{g_1}{8\pi^2} (\bar{\chi} \sigma_{\mu\nu} \chi) B_{\mu\nu} \\ &= \frac{e}{8\pi^2} (\bar{\chi} \sigma_{\mu\nu} \chi) F_{\mu\nu} - \frac{g_1 s_w}{8\pi^2} (\bar{\chi} \sigma_{\mu\nu} \chi) Z_{\mu\nu} \end{aligned} \quad (B5)$$

where, e is the electric charge given by $g_1 c_w$; c_w and s_w are the cosine and sine of the Weinberg angle respectively. Since we ignore the Z-channel in our analysis due to its negligibly available invisible width, we choose to work only with the photon vertex. According to eqn.(B4), c does not evolve; hence, the evolution of this vertex is entirely governed by the SM-evolution of e which is given as follows [92]:

$$e^2 = \frac{\hat{e}^2(M_Z)}{1 + (\hat{\alpha}/\alpha) \Delta \hat{\alpha}(M_Z^2)} \quad (B6)$$

where, \hat{e} and $\hat{\alpha}$ are the \overline{MS} electric charge and the QED coupling constant respectively. $\Delta\hat{\alpha}(M_Z^2)$ is a function expressed in terms of photon polarization functions. After calculation of 2-loop electroweak contribution to the Thomson scattering amplitude, the values $\alpha^{-1}(M_Z)$ has been found at different scales as shown in Table(II).

$\mu(\text{GeV})$	$\alpha^{-1}(\mu)$
91.187	128.122
300	127.369
500	127.046
800	126.748
1000	126.607

TABLE II. $\alpha^{-1}(\mu)$ computed at different scales with 2-loop electroweak corrections [92].

C. Model-Independent Cross-Section Analysis

We present here a model-independent work that provides the production rate of dark states originating from neutral unflavored mesons that can serve as inputs for a broad class of BSM scenarios. We equate the branching ratio of decaying mesons into $\chi\bar{\chi}$ pairs to their invisible branching ratio while pseudoscalar mesons need special treatment due to their three-body decays that demands the input of differential branching ratio for accurate analysis. For a model independent analysis, we assume the modulus squared of amplitude, $|\mathcal{M}|^2$ is a constant and then proceed to find the differential branching ratio to be:

$$\frac{dBR(P \rightarrow \gamma\chi\bar{\chi})}{dq^2 d\cos\theta} = \frac{1}{512M\pi^3} |\mathcal{M}|^2 \sqrt{1 - \frac{4m_\chi^2}{q^2}} \left(1 - \frac{q^2}{M^2}\right) \quad (\text{C1})$$

where, M is the mass of the decaying pseudoscalar meson, q is the squared invariant mass of the $\chi\bar{\chi}$ pair, θ is the angle between direction of p_χ in $\chi\bar{\chi}$ -pair rest frame and $p_\chi + p_{\bar{\chi}}$ in the rest frame of the meson. $|\mathcal{M}|^2 = \epsilon^2$ takes upon an allowed range of values to keep the branching fraction of the pseudoscalar mesons within the experimental bounds on invisible decays. With the above mentioned information, we plot the production rates for this model-independent scenario with $\epsilon = 1$ for π^0 , η and η' in Fig.(13).

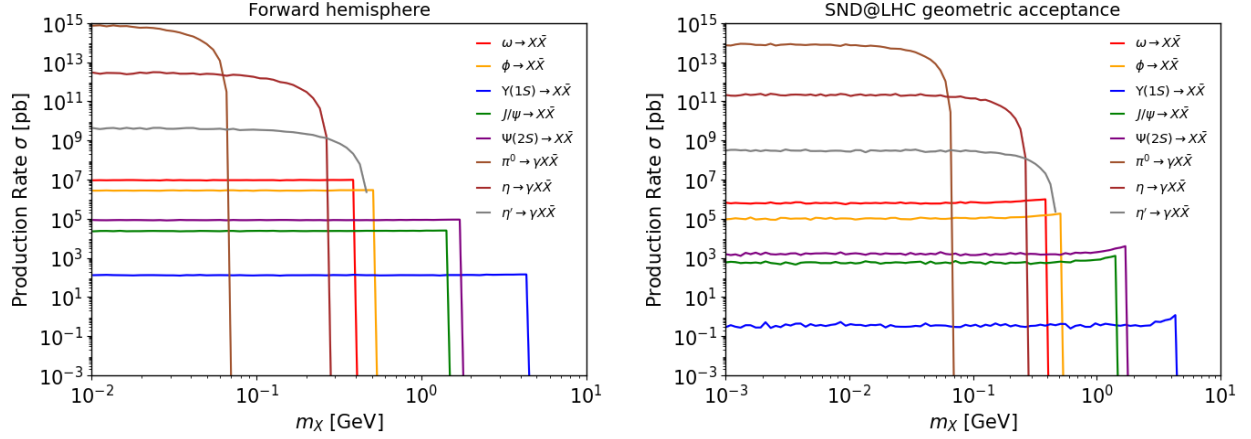


FIG. 13. Production rate of $\chi\bar{\chi}$ -pairs in (Left) the forward half-hemisphere and (Right) in the geometric acceptance of $7.2 < \eta < 8.4$.

As stated above, ϵ can only take values at different values of m_χ that keep the decays of pseudoscalar mesons into χ and $\bar{\chi}$ within their corresponding invisible branching ratios as shown in Fig.(14).

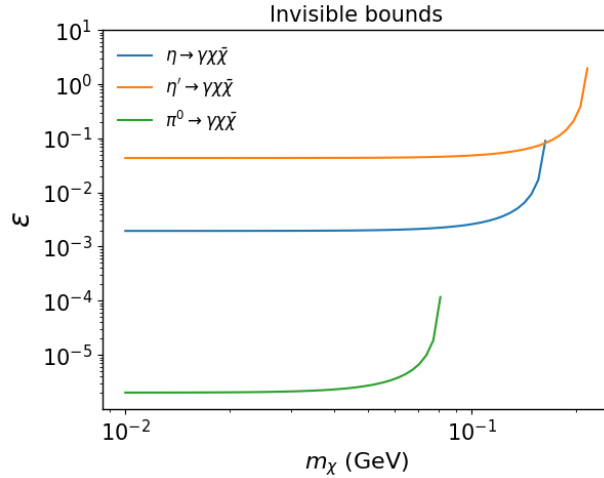


FIG. 14. Model-independent invisible bounds imposed by pseudoscalar invisible branching ratios.

[1] J.L. Feng et al., *The Forward Physics Facility at the High-Luminosity LHC*, *J. Phys. G* **50** (2023) 030501 [2203.05090].

[2] FPF WORKING GROUPS collaboration, *The Forward Physics Facility at the Large Hadron Collider*, 3, 2025 [2503.19010].

[3] L.A. Anchordoqui et al., *The Forward Physics Facility: Sites, experiments, and physics potential*, *Phys. Rept.* **968** (2022) 1 [2109.10905].

[4] J. Adhikary et al., *Scientific program for the Forward Physics Facility*, *Eur. Phys. J. C* **85** (2025) 430 [2411.04175].

[5] FPF collaboration, *Letter of Intent: The Forward Physics Facility*, 2510.26260.

[6] R. Harnik and G.D. Kribs, *An Effective Theory of Dirac Dark Matter*, *Phys. Rev. D* **79** (2009) 095007 [0810.5557].

[7] C. Han, M. López-Ibáñez, B. Peng and J.M. Yang, *Dirac dark matter in $u(1)_{bl}$ with the stueckelberg mechanism*, *Nuclear Physics B* **959** (2020) 115154.

[8] C.E. Yaguna and Ó. Zapata, *Singlet dirac dark matter streamlined*, *Journal of Cosmology and Astroparticle Physics* **2024** (2024) 049.

[9] K. Sigurdson, M. Doran, A. Kurylov, R.R. Caldwell and M. Kamionkowski, *Dark-matter electric and magnetic dipole moments*, *Phys. Rev. D* **70** (2004) 083501.

[10] G. D'Ambrosio, S. Chatterjee, R. Laha and S.K. Vempati, *Freezing in with lepton flavored fermions*, *SciPost Physics* **11** (2021) 006.

[11] A. Ibarra, M. Reichard and G. Tomar, *Probing dark matter electromagnetic properties in direct detection experiments*, *JCAP* **02** (2025) 072 [2408.15760].

[12] E. Masso, S. Mohanty and S. Rao, *Dipolar Dark Matter*, *Phys. Rev. D* **80** (2009) 036009 [0906.1979].

[13] G. Acampora, C. Ahdida, R. Albanese, C. Albrecht, A. Alexandrov, M. Andreini et al., *SND@LHC: the scattering and neutrino detector at the LHC*, *Journal of Instrumentation* **19** (2024) P05067.

[14] C. Ahdida, M. De Magistris, M. Gorshenkov, E. Zaffaroni, L. Dedenko, M. Chernyavskiy et al., *SND@LHC-Scattering and Neutrino Detector at the LHC*, Tech. Rep. CERN-LHCC-2021-003, LHCC-P-016, CERN, Geneva (2021).

[15] A. Boyarsky, O. Mikulenko, M. Ovchynnikov and L. Shchutska, *Searches for new physics at SND@LHC*, *JHEP* **03** (2022) 006 [2104.09688].

[16] B. Batell, J.L. Feng and S. Trojanowski, *Detecting dark matter with far-forward emulsion and liquid argon detectors at the LHC*, *Phys. Rev. D* **103** (2021) 075023.

[17] Y.G. Kim, K.Y. Lee and S.-h. Nam, *Novel search for light dark photon in the forward experiments at the LHC*, *The European Physical Journal C* **84** (2024) 1050.

[18] SHiP collaboration, *A facility to Search for Hidden Particles (SHiP) at the CERN SPS*, 1504.04956.

[19] M. Al-Turany, D. Bertini, R. Karabowicz, D. Kresan, P. Malzacher, T. Stockmanns et al., *The FairRoot framework*, *Journal of Physics: Conference Series* **396** (2012) 022001.

[20] C. Andreopoulos et al., *The GENIE Neutrino Monte Carlo Generator*, *Nucl. Instrum. Meth. A* **614** (2010) 87 [0905.2517].

[21] L.B. Auerbach, R.L. Burman, D.O. Caldwell, E.D. Church, J.B. Donahue, A. Fazely et al., *Measurement of electron-neutrino electron elastic scattering*, *Physical Review D* **63** (2001) .

[22] W.J. Marciano and Z. Parsa, *Neutrino electron scattering theory*, *J. Phys. G* **29** (2003) 2629 [hep-ph/0403168].

[23] J.A. Formaggio and G.P. Zeller, *From eV to EeV: Neutrino cross sections across energy scales*, *Rev. Mod. Phys.* **84** (2012) 1307.

[24] O. Tomalak and R.J. Hill, *Theory of elastic neutrino-electron scattering*, *Phys. Rev. D* **101** (2020) 033006.

[25] J. Alwall, R. Frederix, S. Frixione, V. Hirschi, F. Maltoni, O. Mattelaer et al., *The automated computation of tree-level and next-to-leading order differential cross sections, and their matching to parton shower simulations*, *Journal of High Energy Physics* **2014** (2014) 1.

[26] A. Alloul, N.D. Christensen, C. Degrande, C. Duhr and B. Fuks, *FeynRules 2.0 A complete toolbox for tree-level phenomenology*, *Computer Physics Communications* **185** (2014) 22502300.

[27] F. Kling and S. Trojanowski, *Forward experiment sensitivity estimator for the LHC and future hadron colliders*, *Phys. Rev. D* **104** (2021) 035012 [2105.07077].

[28] E. Conte, B. Fuks and G. Serret, *MadAnalysis 5, A User-Friendly Framework for Collider Phenomenology*, *Comput. Phys. Commun.* **184** (2013) 222 [1206.1599].

[29] X. Chu, J.-L. Kuo and J. Pradler, *Dark sector-photon interactions in proton-beam experiments*, *Phys. Rev. D* **101** (2020) 075035 [2001.06042].

[30] PARTICLE DATA GROUP collaboration, *Review of particle physics*, *Phys. Rev. D* **110** (2024) 030001.

[31] HPQCD collaboration, *B-meson decay constants: a more complete picture from full lattice*

QCD, *Phys. Rev. D* **91** (2015) 114509 [1503.05762].

[32] Q. Chang, X.-N. Li, X.-Q. Li and F. Su, *Decay constants of pseudoscalar and vector mesons with improved holographic wavefunction*, *Chin. Phys. C* **42** (2018) 073102 [1805.00718].

[33] R.M. Barnett, C.D. Carone, D.E. Groom, T.G. Trippe, C.G. Wohl, B. Armstrong et al., *Review of particle physics*, *Phys. Rev. D* **54** (1996) 1.

[34] T. Pierog, I. Karpenko, J.M. Katzy, E. Yatsenko and K. Werner, *EPOS LHC: Test of collective hadronization with data measured at the CERN Large Hadron Collider*, *Phys. Rev. C* **92** (2015) 034906.

[35] R. Ulrich, T. Pierog and C. Baus, *Cosmic Ray Monte Carlo Package, CRMC*, Zenodo (2021)

.

[36] C. Bierlich, S. Chakraborty, N. Desai, L. Gellersen, I. Helenius, P. Ilten et al., *A comprehensive guide to the physics and usage of PYTHIA 8.3*, 2022.

[37] R. Aaij, B. Adeva, M. Adinolfi, A. Affolder, Z. Ajaltouni, S. Akar et al., *Measurement of forward J/ψ production cross-sections in pp collisions at $\sqrt{s} = 13$ TeV*, *Journal of High Energy Physics* **2015** (2015) 172.

[38] R. Aaij, C.A. Beteta, B. Adeva, M. Adinolfi, C.A. Aidala, Z. Ajaltouni et al., *Measurement of $\psi(2S)$ production cross-sections in proton-proton collisions at $\sqrt{s} = 7$ and 13 TeV*, *The European Physical Journal C* **80** (2020) 185.

[39] R. Aaij, B. Adeva, M. Adinolfi, Z. Ajaltouni, S. Akar, J. Albrecht et al., *Measurement of Υ production in pp collisions at $\sqrt{s}=13$ TeV*, *Journal of High Energy Physics* **2018** (2018) 134.

[40] F. Kling, J.-L. Kuo, S. Trojanowski and Y.-D. Tsai, *FLArE up dark sectors with EM form factors at the LHC forward physics facility*, *Nucl. Phys. B* **987** (2023) 116103 [2205.09137].

[41] X. Chu, J. Pradler and L. Semmelrock, *Light dark states with electromagnetic form factors*, *Phys. Rev. D* **99** (2019) 015040 [1811.04095].

[42] LUX COLLABORATION collaboration, *Results from a Search for Dark Matter in the Complete LUX Exposure*, *Phys. Rev. Lett.* **118** (2017) 021303.

[43] PANDAX-II COLLABORATION collaboration, *Dark Matter Results from 54-Ton-Day Exposure of PandaX-II Experiment*, *Phys. Rev. Lett.* **119** (2017) 181302.

[44] XENON COLLABORATION 7 collaboration, *Dark Matter Search Results from a One Ton-Year Exposure of XENON1T*, *Phys. Rev. Lett.* **121** (2018) 111302.

[45] DARKSIDE COLLABORATION collaboration, *Low-Mass Dark Matter Search with the*

*DarkSide-50 Experiment, Phys. Rev. Lett. **121** (2018) 081307.*

[46] SUPERCDMS COLLABORATION collaboration, *Low-mass dark matter search with CDMSlite, Phys. Rev. D* **97** (2018) 022002.

[47] CDEX COLLABORATION collaboration, *Limits on light WIMPs with a germanium detector at 177 eVee threshold at the China Jinping Underground Laboratory, Phys. Rev. D* **90** (2014) 032003.

[48] CDEX COLLABORATION collaboration, *First results on low-mass WIMPs from the CDEX-1 experiment at the China Jinping underground laboratory, Phys. Rev. D* **88** (2013) 052004.

[49] CDEX COLLABORATION collaboration, *Limits on light weakly interacting massive particles from the CDEX-1 experiment with a p-type point-contact germanium detector at the China Jinping Underground Laboratory, Phys. Rev. D* **90** (2014) 091701.

[50] CDEX COLLABORATION collaboration, *Search of low-mass WIMPs with a p-type point contact germanium detector in the CDEX-1 experiment, Phys. Rev. D* **93** (2016) 092003.

[51] L.-T. Yang, H.-B. Li, Q. Yue, K.-J. Kang, J.-P. Cheng, Y.-J. Li et al., *Limits on light WIMPs with a 1 kg-scale germanium detector at 160 eVee physics threshold at the China Jinping Underground Laboratory, Chinese Physics C* **42** (2018) 023002.

[52] CDEX COLLABORATION collaboration, *Limits on Light Weakly Interacting Massive Particles from the First 102.8 kg × day Data of the CDEX-10 Experiment, Phys. Rev. Lett.* **120** (2018) 241301.

[53] H. Jiang et al., *Performances of a prototype point-contact germanium detector immersed in liquid nitrogen for light dark matter search, Sci. China Phys. Mech. Astron.* **62** (2019) 31012 [1810.08808].

[54] CDEX COLLABORATION collaboration, *Search for Light Weakly-Interacting-Massive-Particle Dark Matter by Annual Modulation Analysis with a Point-Contact Germanium Detector at the China Jinping Underground Laboratory, Phys. Rev. Lett.* **123** (2019) 221301.

[55] CDEX COLLABORATION collaboration, *Constraints on Spin-Independent Nucleus Scattering with sub-GeV Weakly Interacting Massive Particle Dark Matter from the CDEX-1B Experiment at the China Jinping Underground Laboratory, Phys. Rev. Lett.* **123** (2019) 161301.

[56] CDEX COLLABORATION collaboration, *Studies of the Earth shielding effect to direct dark*

matter searches at the China Jinping Underground Laboratory, *Phys. Rev. D* **105** (2022) 052005.

[57] CDEX COLLABORATION collaboration, *Constraints on Spin-Independent Nucleus Scattering with sub-GeV Weakly Interacting Massive Particle Dark Matter from the CDEX-1B Experiment at the China Jinping Underground Laboratory*, *Phys. Rev. Lett.* **123** (2019) 161301.

[58] CRESST collaboration, *Results on MeV-scale dark matter from a gram-scale cryogenic calorimeter operated above ground*, *Eur. Phys. J. C* **77** (2017) 637 [1707.06749].

[59] SENSEI COLLABORATION collaboration, *SENSEI: Direct-Detection Results on sub-GeV Dark Matter from a New Skipper CCD*, *Phys. Rev. Lett.* **125** (2020) 171802.

[60] DAMIC COLLABORATION collaboration, *Constraints on Light Dark Matter Particles Interacting with Electrons from DAMIC at SNOLAB*, *Phys. Rev. Lett.* **123** (2019) 181802.

[61] EDELWEISS COLLABORATION collaboration, *First Germanium-Based Constraints on Sub-MeV Dark Matter with the EDELWEISS Experiment*, *Phys. Rev. Lett.* **125** (2020) 141301.

[62] D.W. Amaral, T. Aralis, T. Aramaki, I.J. Arnquist, E. Azadbakht, S. Banik et al., *Constraints on low-mass, relic dark matter candidates from a surface-operated SuperCDMS single-charge sensitive detector*, *Phys. Rev. D* **102** (2020) 091101.

[63] R. Agnese, T. Aralis, T. Aramaki, I.J. Arnquist, E. Azadbakht, W. Baker et al., *First Dark Matter Constraints from a SuperCDMS Single-Charge Sensitive Detector*, *Phys. Rev. Lett.* **121** (2018) 051301.

[64] XENON COLLABORATION collaboration, *Light Dark Matter Search with Ionization Signals in XENON1T*, *Phys. Rev. Lett.* **123** (2019) 251801.

[65] R. Essig, T. Volansky and T.-T. Yu, *New constraints and prospects for sub-GeV dark matter scattering off electrons in xenon*, *Phys. Rev. D* **96** (2017) 043017.

[66] THE DARKSIDE COLLABORATION collaboration, *Constraints on Sub-GeV Dark-Matter–Electron Scattering from the DarkSide-50 Experiment*, *Phys. Rev. Lett.* **121** (2018) 111303.

[67] R. Essig, A. Manalaysay, J. Mardon, P. Sorensen and T. Volansky, *First Direct Detection Limits on Sub-GeV Dark Matter from XENON10*, *Phys. Rev. Lett.* **109** (2012) 021301.

[68] PANDAX-II COLLABORATION collaboration, *Search for Light Dark Matter–Electron*

*Scattering in the PandaX-II Experiment, Phys. Rev. Lett. **126** (2021) 211803.*

[69] T. Emken, R. Essig, C. Kouvaris and M. Sholapurkar, *Direct detection of strongly interacting sub-GeV dark matter via electron recoils, Journal of Cosmology and Astroparticle Physics* **2019** (2019) 070.

[70] SENSEI COLLABORATION collaboration, *SENSEI: Direct-Detection Constraints on Sub-GeV Dark Matter from a Shallow Underground Run Using a Prototype Skipper CCD, Phys. Rev. Lett. **122** (2019) 161801.*

[71] CDEX collaboration, *Constraints on Sub-GeV Dark Matter–Electron Scattering from the CDEX-10 Experiment, Phys. Rev. Lett. **129** (2022) 221301* [2206.04128].

[72] H. An, M. Pospelov, J. Pradler and A. Ritz, *Directly Detecting MeV-Scale Dark Matter Via Solar Reflection, Phys. Rev. Lett. **120** (2018) 141801.*

[73] H. An, H. Nie, M. Pospelov, J. Pradler and A. Ritz, *Solar reflection of dark matter, Phys. Rev. D **104** (2021) 103026* [2108.10332].

[74] CDEX COLLABORATION collaboration, *Experimental Limits on Solar Reflected Dark Matter with a New Approach on Accelerated-Dark-Matter–Electron Analysis in Semiconductors, Phys. Rev. Lett. **132** (2024) 171001.*

[75] T. Emken, *Solar reflection of light dark matter with heavy mediators, Phys. Rev. D **105** (2022) 063020.*

[76] R. Essig, J. Mardon and T. Volansky, *Direct detection of sub-GeV dark matter, Phys. Rev. D **85** (2012) 076007.*

[77] B. Aubert, A. Bazan, A. Boucham, D. Boutigny, I. De Bonis, J. Favier et al., *The BABAR detector, Nuclear Instruments and Methods in Physics Research Section A: Accelerators, Spectrometers, Detectors and Associated Equipment* **479** (2002) 1.

[78] CHARMII collaboration, *A detector for the study of neutrino-electron scattering, Nucl. Instrum. Methods Phys. Res., A* **278** (1989) 670.

[79] R. Ball et al., *The Neutrino Beam Dump Experiment at Fermilab (E613), eConf* **C801002** (1980) 172.

[80] C. Athanassopoulos, L. Auerbach, D. Bauer, R. Bolton, R. Burman, I. Cohen et al., *The liquid scintillator neutrino detector and LAMPF neutrino source, Nuclear Instruments and Methods in Physics Research Section A: Accelerators, Spectrometers, Detectors and Associated Equipment* **388** (1997) 149.

[81] A. Aguilar-Arevalo, C. Anderson, L. Bartoszek, A. Bazarko, S. Brice, B. Brown et al., *The MiniBooNE detector, Nuclear Instruments and Methods in Physics Research Section A: Accelerators, Spectrometers, Detectors and Associated Equipment* **599** (2009) 28.

[82] THE MINIBOONE-DM COLLABORATION collaboration, *Dark matter search in nucleon, pion, and electron channels from a proton beam dump with MiniBooNE*, *Phys. Rev. D* **98** (2018) 112004.

[83] X. Chu, J.-L. Kuo and J. Pradler, *Dark sector-photon interactions in proton-beam experiments*, *Phys. Rev. D* **101** (2020) 075035.

[84] Y. Zhang, M. Song and L. Chen, *Dark states with electromagnetic form factors at electron colliders*, *Phys. Rev. D* **107** (2023) 055023.

[85] T. Trickle, Z. Zhang and K.M. Zurek, *Detecting Light Dark Matter with Magnons*, *Phys. Rev. Lett.* **124** (2020) 201801.

[86] C. Arina, A. Cheek, K. Mimasu and L. Pagani, *Light and darkness: consistently coupling dark matter to photons via effective operators*, *The European Physical Journal C* **81** (2021) 223.

[87] D. Abbaneo, E. Zaffaroni, M. Chernyavskiy, V. Tioukov, M. Spurio, F. Cindolo et al., *AdvSND, The Advanced Scattering and Neutrino Detector at High Lumi LHC Letter of Intent*, Tech. Rep. CERN-LHCC-2024-007, LHCC-I-040, CERN, Geneva (2024).

[88] SND@LHC collaboration, *Input from the SND@LHC collaboration to the 2026 Update to the European Strategy for Particle Physics*, 2503.24233.

[89] D. Abbaneo, M. De Magistris, E. Zaffaroni, M. Chernyavskiy, M. Spurio, F. Cindolo et al., *SND@ HL-LHC, Scattering and Neutrino Detector in Run 4 of the LHC*, Tech. Rep. CERN-LHCC-2025-004, LHCC-P-026, CERN, Geneva (2025).

[90] SND@LHC collaboration, *Input from the SND@LHC collaboration to the 2026 Update to the European Strategy for Particle Physics*, 2503.24233.

[91] F. Bishara, J. Brod, B. Grinstein and J. Zupan, *Renormalization group effects in dark matter interactions*, *Journal of High Energy Physics* **2020** (2020) .

[92] G. Degrassi and A. Vicini, *Two-loop renormalization of the electric charge in the standard model*, *Phys. Rev. D* **69** (2004) 073007.